PNAS

www.pnas.org

Supplementary Information for

Background-free dual-mode optical and ^{13}C magnetic resonance imaging in diamond particles

Xudong Lv, Jeffrey H. Walton, Emanuel Druga, Fei Wang, Alessandra Aguilar, Tommy McKnelly, Raffi Nazaryan, Fanglin Linda Liu, Lan Wu, Olga Shenderova, Daniel B. Vigneron, Carlos A. Meriles, Jeffrey A. Reimer, Alexander Pines

Ashok Ajoy.
E-mail: ashokaj@berkeley.edu

This PDF file includes:

Supplementary text
Figs. S1 to S12 (not allowed for Brief Reports)
Tables S1 to S2 (not allowed for Brief Reports)
SI References

Supporting Information Text

1. Three imaging regimes

The combination of optical and MR imaging, acquired simultaneously from diamond particles consisting of NV centers and hyperpolarized ^{13}C nuclei, allows for enhancements in imaging in several different contexts. In particular, we considered three regimes of imaging (Table S1):

Particular specifics	Regime I	Regime II	Regime III
Primary mode	Optical imaging	Hyperpolarized MRI	Accelerated dual-mode
Secondary mode	Hyperpolarized MRI	Optical imaging	imaging protocol
Operating regime	Deep in scattering media	Shallow or in non-scattering media	Shallow or in non-scattering media
Primary mode SNR	$\propto \gamma_0 \cdot e^{-\alpha_i d}e^{-\alpha_\epsilon d}$	$\propto P_i(\Delta x_{\mathrm{mri}})^2 \cdot \sqrt{T}$	
Dual mode SNR	$\propto e^{-\alpha_i d}$	$\propto \frac{\mathrm{FOV}}{\Delta x_{\mathrm{optics}}^2}P_i(\Delta x_{\mathrm{optics}})^2 \cdot \sqrt{T/\frac{\mathrm{FOV}}{\Delta x_{\mathrm{optics}}^2}}$	$\propto \sqrt{T/(1-s)^{1/2}}$ [3]
SNR gain	$1/\gamma_0 \cdot e^{\alpha_\epsilon d}$	$\frac{\sqrt{FOV}\Delta x_{\mathrm{optics}}}{\Delta x_{\mathrm{mri}}^2}$	$\propto 1/(1-s)^{1/4}$ [7]
Primary mode SNR (example)	$4.4\times10^{-3}\sqrt{\mathrm{Hz}}$ [2]	$0.63\sqrt{\mathrm{Hz}}$ [4]	$47.5\sqrt{\mathrm{Hz}}$ [4]
Dual mode SNR (example)	$1.1\times10^{-2}\sqrt{\mathrm{Hz}}$ [2]	$6.3\sqrt{\mathrm{Hz}}$ [5]	
SNR gain (example)	2.5	10	5 [6][7]
Primary mode resolution δx_p	$\propto d$	δx_{mri}	$\delta x_{\mathrm{optics}}$
Dual mode resolution δx_d	$\sim \frac{1}{\gamma G_{max}\tau}$	$\delta x_{\mathrm{optics}}$	
Resolution gain $\frac{\delta x_p}{\delta x_d}$	$\propto d$	$\frac{\delta x_{\mathrm{mri}}}{\delta x_{\mathrm{optics}}}$	N.A.
Resolution limit	$\sim \frac{1}{\gamma G_{max}\tau} \ (\sim 1\mu m$ [8]$)$	$\frac{\lambda}{2}$	$\frac{\lambda}{2}$
Primary mode resolution (example)	$1200\mu m$ [3]	$640\mu m$ [4]	$40\mu m$ [4]
Dual mode resolution (example)	$640\mu m$ [4]	$40\mu m$ [4]	
Resolution gain (example)	1.875	16	N.A.
Power reduction [1]	$1/\gamma_0 \cdot e^{\alpha_\epsilon d}$	$\frac{\sqrt{FOV}\Delta x_{\mathrm{optics}}}{\Delta x_{\mathrm{mri}}^2}$	$\propto 1/(1-s)^{1/2}$
Power reduction (example)	2.5	10	25 [6]
Background suppression	MRI can suppress optical background	Minimal background in ^{13}C MRI	Field modulation can suppress optical background [9]

[a] Power reduction defined as the ratio between the power required by single primary mode and dual-mode approach to achieve certain SNR.

[b] Extrapolated from experimental number to $d = 3$mm, using loss coefficient 13.5 cm^{-1} for 532nm laser and 12.1 cm^{-1} for 650nm fluorescence in a scattering media (See Section A, diamond mass ~ 40mg). The coefficients are calculated based on fatty tissue data in (1).

[c] Extrapolated from mian Figure 1, and taking a depth of 15mm.

[d] Taken from the dual-mode experiment demonstrated in main Figure1 (See Section A).

[e] Extrapolated from the experiment demonstrated in main Figure 1, assuming FOV $= (6.4$mm$)^2$ (Details see Section B).

[f] Obtained from main Figure 4 when assuming $(1 - s) = 0.9 \times 10^{-3}$.

[g] The SNR gain in the third mode is defined as the ratio between dual-mode SNR and optical SNR.

[h] Based on gyromagnetic ratio of ^{13}C, G_{max} can be up to 60 T/m in (2), and $\tau \sim T_2 \approx 1$ms.

[i] See main Figure 3.

Table S1. Dual-mode imaging regimes from a combination of optics and MRI. Regime I and II consider optics and MRI being primary imaging modes in scattering and scattering-free media respectively. Regime III considers sampling in both imaging dimensions as elucidated in the algorithm of dual-mode imaging. Red color indicates parameters where image enhancements can be gained via dual-mode combination. For clarity, the variables here refer to γ_0, ratio between optical SNR and MR SNR at $d = 0$; P_i incident power density; Δx pixel size; $\alpha_i, \alpha_\epsilon$ incident and emission light loss coefficient, including scattering and attenuation; d object depth; T imaging time; $\Delta x_{\mathrm{optics}}, \Delta x_{\mathrm{mri}}$, pixel size for optical and MRI; FOV, field of view; s, sparsity, the proportion of dark pixels.

A. Regime I: Optical imaging as the primary imaging mode. Let us consider the first regime where optical imaging is the primary mode employed the diamond particles, but one has the additional capability to acquire the image through MRI.

Operating Regime – This mode corresponds to the operating regime where optical imaging is the primary mode, and when optical scattering prevails, an additional MR modality provides better SNR, resolution, imaging depth and imaging power reduction. In non-scattering cases, optics preserves advantages over MRI if objects are shallow. However, in scattering media, the SNR and resolution of the optics deteriorates rapidly with increasing of depth (depth $>\sim$ mm). On the other hand, MRI via RF signal acquisition that is independent of depth, offers a complementary approach to improve image qualities and to extend the accessible depth of this imaging regime.

Under the assumption of objects buried in scattering media, the *critical depth* where MRI shows equal efficacy with optics depends on the scattering properties. For instance, if we take the scattering media describe in Table I, the critical depths are ~ 2 mm for SNR and ~ 6 mm for resolution (details see Section C and D). This suggests that MR starts to play a critical role when imaging objects are below such critical depths.

Signal to noise – We here analyze the SNR enhanced by the secondary mode – MRI, which is acquired by RF wave that immunes to scattering by media, such as tissue. The SNR of an image is determined by factors associated with the specific experimental settings. We first study the expressions of the optical SNR in terms of incident power density P_i, pixel size Δx, sample depth d, as well as average time T. Within the linear regime of power dependency, the image SNR of optics is proportional to:

$$SNR \propto \gamma_0 P_i(\Delta x)^2 \cdot e^{-\alpha_i d}e^{-\alpha_\epsilon d}\sqrt{T} \qquad [1]$$

where γ_0 is the SNR ratio between optics and MRI at 0 depth, and $(\Delta x)^2$ accounts for the cumulative signal in a pixel area, and $e^{-\alpha_i d}$, $e^{-\alpha_\epsilon d}$ are factors representing "round-trip" scattering loss of incident and emission light. In the shot noise limited regime caused by attenuation and

Xudong Lv, Jeffrey H. Walton, Emanuel Druga, Fei Wang, Alessandra Aguilar, Tommy McKnelly, Raffi Nazaryan, Fanglin Linda Liu, Lan Wu, Olga Shenderova, Daniel B. Vigneron, Carlos A. Meriles, Jeffrey A. Reimer, Alexander Pines

scattering, SNR can be increased by averaging, leading to the factor $\sqrt{T}$ in the expression. Assuming the luminescence is applied uniformly across the entire sample, we can use the total optical power P_{tot} and the imaging field of view FOV to substitute P_i and rewrite SNR as: $SNR \propto \gamma_0 \frac{P_{tot}}{FOV}(\Delta x)^2 \cdot e^{-\alpha_i d}e^{-\alpha_\epsilon d}\sqrt{T}$. In the experiment of main Figure 1A, the SNR of the optical imaging in Figure 1E is 12, as P_i=320 mW/mm^2 , Δx=40 μm, d=0, T = 0.1s.

Similarly, for an optically hyperpolarized MR image, we find the SNR expression is similar to an optical image in terms of nuclear polarization to be P_{nuclei}: $SNR \propto P_{nuclei}(\Delta x)^2 \cdot e^{-\alpha_i d}\sqrt{T}$ Typically, in the linear regime of optical power dependence:

$$SNR \propto P_i(\Delta x)^2 \cdot e^{-\alpha_i d}\sqrt{T} \qquad [2]$$

where the $e^{-\alpha_i d}$ factor represents the scattering loss of the incident light. In the experiment of Figure 1, $P_{nuclei} \sim 0.3\%$, P_i=80 mW/mm^2 (P_{tot}=1W), Δx= 160μm, d=0, T = 0.8s. The image in Figure 1F presents a SNR of 4.

In order to fairly compare the SNR of the two modes, we need to rescale it based on power and normalize it with respect to imaging time. For example, under the same excitation power with MR imaging (80 mW/mm^2), the optical SNR in main Figure 1E is rescaled to 3.0. This corresponds to an optical SNR of $9.5\sqrt{\text{Hz}}$ when further normalized by acquisition time (0.1 s). Similarly, normalizing the SNR of MRI, we obtain $0.63\sqrt{\text{Hz}}$, with consideration of 40s dead time to hyperpolarize the sample. In this case, the ratio between the two SNRs is $\gamma_0 = 15$.

Now we analyze how MRI can provide a SNR gain when $d > \sim$mm. Comparing Equation 1 with Equation 2, we see a SNR gain of $1/\gamma_0 \cdot e^{\alpha_\epsilon d}$ when implementing the secondary mode. With $d = 0$ as a benchmark (in Figure 1), we derive the SNR of the scenario where $d \neq 0$ based on the SNR formulas above in Equation 1. If we take objects buried under 3 mm as an example, assuming we have the same experimental setup, the ratio of time-normalized SNR between MRI and optics is $1/\gamma_0 \cdot e^{\alpha_\epsilon d} = 2.5$.

Resolution – In this regime, the MR modality compensates the resolution degradation of the primary mode optics. The resolution of MRI depends on gyromagnetic ratio γ, maximum gradient of the imager G_{max}, and echo time τ: ,

$$\delta x \propto \frac{1}{\gamma G_{max}\tau} \qquad [3]$$

which is irrelevant to object depth. However, optical resolution strongly depends on scattering distortion; δx can be simulated by integrating the Wigner function assuming the scattering media is homogeneous, and the linear approximation holds in this regime (see Fig. S3):

$$\delta x \propto d \qquad [4]$$

Similarly, taking the ratio between Equation (3) and Equation (4), the resolution gain enabled by MRI scales linearly with d. In an example case of $d = 15$mm in a typical media (see Section IIIC), MRI produces better resolution (640μm) than optics (1200μm).

The ultimate resolution limit of the two modalities are different. Optical imaging is set by the diffraction limit $\delta x = \frac{\lambda}{2} \sim 0.3\mu$m, where λ is the wavelength of the fluorescent light. In the practical case (Figure 1E), optical pixel size $\Delta x = 40\mu$m, which is far from the diffraction limit. This is due to low N.A. of the lens and CCD resolution limit. In contrast, as a Fourier imaging technique, MRI resolution is not limited by electromagnetic wave diffraction, though in practical settings, it is normally restricted to low field gradients. Resolution of 1μm is achievable for ^{13}C imaging if the gradient is strong enough as in (2). Note that here we only consider imaging solids where diffusion is not operative.

Imaging Power – We anticipate imaging power reduction by dual-mode imaging in comparison with single mode optics. Imaging power is normally associated with desired SNR. If one expects a certain SNR of the final image, the corresponding imaging power required can be derived based on Equation (1) and Equation (2). The imaging power reduction is $1/\gamma_0 \cdot e^{\alpha_\epsilon d}$.

Without changing the experimental setting as in main Figure 1, to characterize the incident optical power of optics and MRI on an equal footing, we normalize them to the same SNR of $1\sqrt{\text{Hz}}$. The imaging power required for optics and MRI to achieve such SNR is P_i=8.4 mW/mm^2 and 127 mW/mm^2 respectively when d =0. At depth of $d = 3$mm, the ratio between imaging power required for optics and MRI to achieve SNR of 1 is 2.5. This entails that MR modality can provide power reduction in scattering media.

Background Suppression – In this regime, the optical background can be suppressed by MRI considering a minimal background of ^{13}C imaging. In usual cases, background suppression enables us to remove the time-invariant background by modulating the actual signal. As demonstrated in main Figure 3, suppression of the optical background by a factor of 5, and MRI by a factor of 2 is achieved. However, when scattering predominants, the optical modulation may degrade significantly while the secondary mode MRI remains effective. In practice, the ^{13}C background is negligible due to low natural abundance of ^{13}C and low gyromagnetic ratio, so implementing dual-mode imaging can generate background free MRI in this regime. Note that optical background suppression by signal modulation is still valid when scattering is insignificant. It can be applied in noisy settings especially when biological samples emit autofluorescence. In principle, 100 folds of background can be eliminated via our method(3).

B. Regime II: MRI as the primary imaging mode. Now we consider MR imaging as the primary mode, with additional ability to acquire the image through optical means. In this regime, we can employ a pixel-by-pixel excitation to selectively hyperpolarize diamonds within a specific pixel. Imaging such hyperpolarized samples via MR allows us to boost the SNR and resolution of MR images.

Operating Regime – In this regime, MR measures signals from optically resolved pixels at each time and recomposes the signal to form a complete image. To ensure effective high resolution optical illumination, objects have to be shallow (depth $< \sim$ mm) or in non-scattering media.

Signal to noise – The SNR of MR modality in this regime can be enhanced by optics via focusing the illumination beam. If we assume the sample can take certain amount of total power P_{total}, focusing incident light of the same power down to a smaller size Δx^2 equivalently enhances power density P_i in Equation (2) by a factor of $\frac{FOV}{\Delta x_{\text{optics}}^2}$. Here Δx_{optics} is optical resolution or beam size. In the linear regime of optical power dependence, the SNR of a MR image is improved by the same factor with power density enhancement. In addition, we should

Xudong Lv, Jeffrey H. Walton, Emanuel Druga, Fei Wang, Alessandra Aguilar, Tommy McKnelly, Raffi Nazaryan, Fanglin Linda Liu, Lan Wu, Olga Shenderova, Daniel B. Vigneron, Carlos A. Meriles, Jeffrey A. Reimer, Alexander Pines

also take into account that pixel size $(\Delta x)^2$ is reduced by a factor of $\frac{\Delta x_{\mathrm{optics}}^2}{\Delta x_{\mathrm{mri}}^2}$, resulting in less signal to be collected in one measurement. Here Δx_{mri} represents the resolution of a MR image acquired in single mode. Last, scanning through the entire FOV with a fine resolution takes longer time than wide field imaging. The acquisition time $\sqrt{T}$ extends by a factor of $\frac{FOV}{\Delta x_{\mathrm{optics}}^2}$, as more measurements need to be made.

Combining all three factors, the SNR improvement in this regime is $\frac{\sqrt{FOV}\Delta x_{\mathrm{optics}}}{\Delta x_{\mathrm{mri}}^2}$.

If we take the experiment demonstrated in main Figure 1 as an example where $FOV = (6.4\mathrm{mm})^2$, and optical $\Delta x_{\mathrm{optics}} = 40\mu m$, MR $\Delta x_{\mathrm{mri}} = 160\mu m$, this imaging regime empowers up to 10 times SNR improvement. Note that in our assumption, P_{total} stays the same so that P_i is increased, and so as SNR. This holds if the sample takes the incident power as a whole or the heat conductivity is high so that the optical power distributes to the entire sample. In practical cases, we may not be able to increase the power density P_i by that much due to a local power threshold, and the actual SNR improvement may be lower than $\frac{\sqrt{FOV}\Delta x_{\mathrm{optics}}}{\Delta x_{\mathrm{mri}}^2}$.

Resolution – In this regime, MR modality is augmented with optical resolution by focusing down the excitation beam. When optics focuses on certain pixels, only ^{13}C nuclei within this pixel are hyperpolarized. Subsequently we acquire the MR signal only from this pixel with optical resolution. After raster scanning the beam across the entire FOV, we can reconstruct the image with the signals obtained. With such method, MRI resolution can potentially be enhanced by a factor of $\frac{\delta x_{\mathrm{mri}}}{\delta x_{\mathrm{optics}}}$. This is a factor of 16 based on the demonstrated experiment, but a factor of 2×10^3 can be achieved if we focus the beam to diffraction limit, namely $\Delta x_{\mathrm{optics}} = 0.3\mu m$.

Imaging Power – Imaging power can be reduced via efficient power usage in this regime. Based on the analysis in "SNR section", normalizing the SNR to $1\sqrt{\mathrm{Hz}}$ for both single mode MRI and optically resolved MRI, we obtain that the imaging power p_{total} can be reduced by a factor of $\frac{\sqrt{FOV}\Delta x_{\mathrm{optics}}}{\Delta x_{\mathrm{mri}}^2}$. This corresponds to a 10 times reduction in our experimental setting.

Background Suppression – In this regime, we assume the ^{13}C background is minimal because of low natural abundance in a practical setting and the image be immune from background.

C. Regime III: "Dual mode" combined optical and hyperpolarized MRI. Finally, we analyze the regime where optical and MR imaging are combined, leveraging the fact that the two imaging modes sample in real- and k-space simultaneously. In this case, an "accelerated dual mode protocol" (described in main Figure 4) is used, and it produces faster acquisition by reducing the number of sample points.

Operating regime – The gains of combining two imaging modalities arise in the operating regime where objects are shallow (depth $<\sim$ mm) or in non-scattering media to allow relatively good optical SNR and resolution. This is the same as the second imaging regime we described above.

Signal to noise – The "accelerated dual mode protocol" allows for higher normalized SNR than single mode optics resulting from the saving empowered by the protocol. In this regime, the final image is constructed by optical scanning. As a result, the final SNR is ultimately determined by the SNR of the optical imaging. However, the time to acquire an image is shorter by a factor of $\propto 1/(1-s)^{1/2}$ with the accelerated protocol, allowing for a factor of $\propto (1-s)^{1/4}$ SNR enhancement.

For example, in the case illustrated in Figure 4C, if acquisition is accelerated 25 times, the normalized SNR is therefore enhanced by a factor of 5. With the same experimental setting that can achieve single mode optical SNR of $9.5\sqrt{\mathrm{Hz}}$ (analyzed in Section IA), we expect a SNR of $47.5\sqrt{\mathrm{Hz}}$ when combing optics and MRI.

Acceleration – The immediate advantages that the combined optical and MRI imaging can enable is imaging acceleration with respect to simple raster scanning. The acquisition can be accelerated by a factor proportional to $[(1-s)]^{1/2}$. If we take $(1-s) = 0.5\%$ as an example, imaging acceleration is 25 (see main Figure 4C).

Resolution – Optics determines the imaging resolution in this regime as the protocol ends with the optical sampling of real-space. As a result, the protocol can achieve optical resolution, the ultimate limit of which is defined by the diffraction $\delta x = \frac{\lambda}{2} \sim 0.3\mu m$.

Imaging Power – Under this regime, optical power can be better focused on pixels where meaningful objects are located. Total optical power P_{tot} will be reduced due to less measurements being performed in real-space so that less pixels are required to be optically addressed. The power reduction is proportional to $[(1-s)]^{1/2}$. If we use $(1-s) = 0.5\%$ as an example, imaging power reduction is ~ 25 times (see Figure 4).

2. Accelerated dual mode imaging protocol

This section describes the details of the numerical evaluation of the fast imaging protocol in Figure 4 of the main paper. The target image for demonstration (main Figure 4B "Target Image") is a 512×512 high-resolution artificial picture, higher than the target resolution (64×64) to mimic real objects. This real-space image corresponds to a 512×512 k-space dataset (shown for clarity in Fig. S1B). When we perform the fast imaging protocol, a 16×16 region at the center of the k-space is selected to emulate MRI k-space subsampling. This sampled dataset is then zero filled to a form a 64×64 matrix (Figure 4B "Sampled k-Space"), and subsequently Fourier transformed to reconstruct a blurry 64×64 real-space image (Figure 4B "MR Image"). We set a threshold at 0.1 times the mean pixel value, and the pixels with values above the threshold are optically sampled to obtain Figure 4B ("Accelerated Optical Image").

Using the protocol described in Figure. 4A, B, we perform numerical experiments in Figure. 4C-F with randomly generated target objects. Specifically, we randomly place "points" that are round in shape in a 32×32 FOV frame to form target images. This is relevant to diamond tracking and targeting scenarios, where diamonds are small clusters in the FOV. Each point has an intensity of 1, and the background is 0. We can control the number of "points" inserted to the image to vary sparsity s. The simulated results is shown in Figure. 4C, and each data points on the plot of correspond to an average of 30 different experiments with 30 random target images. Each individual experiment follows the protocol described above, with evaluation of acquisition acceleration and image fidelity (i.e. image correlation). We plot the optimized sampling width and total time in Figure. 4D and E.
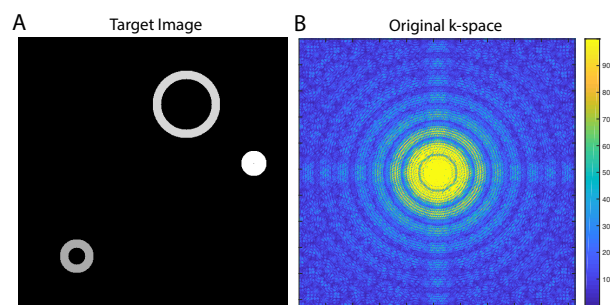
Xudong Lv, Jeffrey H. Walton, Emanuel Druga, Fei Wang, Alessandra Aguilar, Tommy McKnelly, Raffi Nazaryan, Fanglin Linda Liu, Lan Wu, Olga Shenderova, Daniel B. Vigneron, Carlos A. Meriles, Jeffrey A. Reimer, Alexander Pines

A Target Image   B Original k-space

Fig. S1. Target image and corresponding k-space data of exemplary ring-like phantom images in Figure 4 of the main paper. Both spaces have 512 × 512 pixels.

Xudong Lv, Jeffrey H. Walton, Emanuel Druga, Fei Wang, Alessandra Aguilar, Tommy McKnelly, Raffi Nazaryan, Fanglin Linda Liu, Lan Wu, Olga Shenderova, Daniel B. Vigneron, Carlos A. Meriles, Jeffrey A. Reimer, Alexander Pines

In Figure 4F, to characterize the reconstructed image convergence towards the target as optical sampling rate increases, we evaluate the "image correlation" convergence curve. Image correlation is defined as $r = \frac{\sum_{m,n}(A_{mn}-\overline{A})(B_{mn}-\overline{B})}{\sqrt{\left(\sum_{m,n}(A_{mn}-\overline{A})^2\right)\left(\sum_{m,n}(B_{mn}-\overline{B})^2\right)}}$ where A_{mn} and B_{mn} are the intensity of pixel (m,n) in two images A and B (here the reconstructed image and target image respectively). In the simulation of optical sampling, we assume that the pixels are sampled in a certain order based on their intensity. Explicitly, from the coarse reconstructed MR image, the pixels are sorted by their amplitudes, and real-space sampling is performed with a high- to low-amplitude order. Figure. 4F indicates that sampling a few high-intensity pixels will quickly saturate the correlation curve, while smaller ones play less important role.

A. Theoretical model. In this section, we elaborate on the scaling behavior of the algorithm and attempt to generalize the protocol to higher dimensions.

First, let us quantify the blur caused by k-space subsampling. Assuming the original real-space image is $f(x,y)$, then the corresponding k-space function is $\hat{f}(k_x, k_y) = \mathcal{F}(f)$. Assuming a real-space pixel length of $\delta x, \delta y = 1$ and a square FOV, we get $\delta k_x, \delta k_y = \frac{1}{N}$ respectively, where N is the image length in one dimension. If we consider that the sampling in k-space occurs up to ℓ-th order, meaning that we sample a $\ell \times \ell$ window at the center of k-space, this provides a truncated k-space image:

$$\hat{f}_\ell(k_x, k_y) = \hat{f}(k_x, k_y) \cdot \Pi\left(\frac{k_x}{W_{kx}}\right) \cdot \Pi\left(\frac{k_y}{W_{ky}}\right) \qquad [5]$$

where Π is rectangular function with length of $W_{kx} = \delta k_x \cdot \ell$ and $W_{ky} = \delta k_y \cdot \ell$. The signal transformed to real-space image then becomes:

$$f_\ell(x,y) = \mathcal{F}^{-1}(\hat{f}_\ell(k_x, k_y))$$
$$= f(x,y) * [W_{kx}\mathrm{sinc}(W_{kx}x) \cdot W_{ky}\mathrm{sinc}(W_{ky}y)] \qquad [6]$$

where $*$ represents a convolution operation. For simplicity, we consider the case when there is only one single point in real-space, where $f(x,y)$ is effectively approximated by a delta function of unit pixel size in real space. General objects can be linearly constructed from this case. The effective point spread function (psf) is then the product of sinc functions $f_\ell(x,y) = \mathrm{sinc}(W_{kx}x) \cdot \mathrm{sinc}(W_{ky}y) = \mathrm{sinc}(x\delta k\ell) \cdot \mathrm{sinc}(y\delta k\ell)$. This means that truncation in k-space effectively leads to a blurring of the image in real-space (see Fig. S2).

In the protocol, we want to select pixels that are worth to be optically sampled by thresholding the coarse image, and this step determines the effective psf broadening. The threshold we choose here is based on the idea of excluding the shoulder of the psf (Fig. S2B), which is approximately below 0.3 times of the maximum. With such thresholding, we will only select the center peak of the psf (in Fig. S2B) up to a point where $x_0 = 0.75\frac{1}{\delta k\ell}$, because $\mathrm{sinc}(W_{kx}x_0) = 0.3$. Thus, the effective expansion of the real space psf is $r \to r + 0.75\frac{1}{\delta k\ell}$. The optical scan time can be estimated from the area of the psf $\pi(r + 0.75\frac{1}{\delta k\ell})^2$, where we assume one unit area corresponds to one unit time of imaging. Considering both optical and MR imaging, total time:

$$T = \pi n_d \left(r + r_0 \frac{1}{\delta k\ell}\right)^2 + \ell^2 \qquad [7]$$

where n_d is the number of "points" within the FOV assuming the image is sparse enough and the points are not overlapping, and r_0 is conditioned on the thresholding value used in more general cases (here we use $r_0 = 0.75$ for a threshold of 0.3 in our simulations). For a fair comparison, we normalize the time cost against conventional imaging to get $\tau = \frac{T}{N^2}$.

We analyze the relationship between time cost of our protocol τ with respect to the k-space sample order ℓ to identify the optimal sampling strategy. Note here we use s to denote the image sparsity – the portion of the zero-valued pixels. We define the "image occupancy" to be $(1-s) = \frac{1}{N^2}\pi r^2 n_d$. Combining the equations, we have:

$$\tau = (1-s) + \frac{2r_0}{r}\frac{1}{\ell}\left[(1-s)N\right] + \frac{r_0^2}{r^2}\frac{1}{\ell^2}\left[(1-s)N^2\right] + \frac{\ell^2}{N^2} \qquad [8]$$

This equation yields the fitting in main Figure. 4C. We hope to find the minimum time cost $\tau(\ell)$ analytically. Under the assumption of highly sparse images, we take approximations: $(1-s) \to 0$. Given the definition of $1-s$, we also have $(1-s)N \to 0$, and $(1-s)N^2 \to \mathcal{O}(1)$,

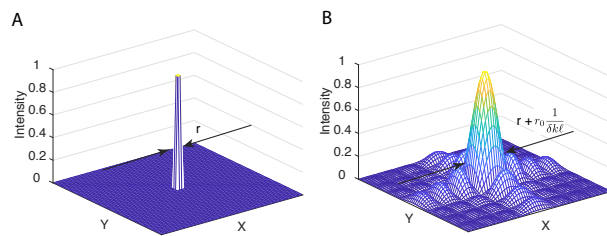$$\tau(\ell) = A\frac{1}{\ell^2} + B\ell^2, \qquad [9]$$

where $A = \frac{r_0^2(1-s)N^2}{r^2}$, and $B = \frac{1}{N^2}$. Let us now derive the corresponding optimal value for ℓ. Taking the derivative of $\tau(\ell)$ to minimize it and identify the optimal sub-sampling size in each dimension ℓ, we get: $\frac{d\tau(\ell)}{d\ell} = -2A\frac{1}{\ell^3} + 2B\ell = 0$. We get $\ell_{opt} = (\frac{A}{B})^{1/4} \propto (1-s)^{1/4}$, and corresponding to an optimal time $\tau = 2(AB)^{1/2} \propto (1-s)^{1/2}$. These formulae, in the limit of $s \to 1$, show a good agreement with both image simulation results (data points in Figure. 4D,E) and numerical optimization results (solid line in Figure. 4D,E), that were obtained numerically without any approximations.

Let us now finally extend these calculations to the case of d dimensional imaging, one can evaluate the relative imaging time under the assumption of high image sparsity:

$$\tau(\ell) = \frac{1}{N^d}[C(d)\pi n_d(r + r_0\frac{N}{\ell})^d + \ell^d] \approx A_d\frac{1}{\ell^d} + B_d\ell^d \qquad [10]$$

where $C(d)$ is a dimension dependent constant that sets the effective d-dimensional volume for instance, $C(3) = \frac{4}{3}\pi$, $C(1) = \pi$, and $A_d = \frac{r_0^d(1-s)N^d}{r^d}$, and $B_d = \frac{1}{N^d}$. We then derive optimal $\ell_{opt,d} = (\frac{A}{B})^{1/2d} \propto (1-s)^{1/2d}$, and optimal $\tau_{opt,d} = 2(AB)^{1/2} \propto (1-s)^{1/2}$. Note that the scaling of optimal relative imaging time τ_{opt} is independent of dimension d.

Kudong Lv, Jeffrey H. Walton, Emanuel Druga, Fei Wang, Alessandra Aguilar, Tommy McKnelly, Raffi Nazaryan, Fanglin Linda Liu, Lan Wu, Olga Shenderova, Daniel B. Vigneron, Carlos A. Meriles, Jeffrey A. Reimer, Alexander Pines

Fig. S2. Blur caused by k-space subsampling. (A) The intensity map of a single point image. (B) The reconstructed point becomes blurred due to k-space subsampling. There are multiple peaks besides the center, following the profile of sinc functions along two dimensions ($\mathrm{sinc}(W_{kx}x) \cdot \mathrm{sinc}(W_{ky}y)$). Thresholding the intensity can exclude higher order peaks.

Xudong Lv, Jeffrey H. Walton, Emanuel Druga, Fei Wang, Alessandra Aguilar, Tommy McKnelly, Raffi Nazaryan, Fanglin Linda Liu, Lan Wu, Olga Shenderova, Daniel B. Vigneron, Carlos A. Meriles, Jeffrey A. Reimer, Alexander Pines

193 Finally, we comment that the imaging acceleration in our case can enable a substantial and concomitant decrease of effective imaging
194 power. This is because the protocol effectively reduces the imaging volume to be probed over. In the demonstration in Figure 4B of the main
195 paper, for instance, the acceleration $\tau \approx 0.073$ corresponds to a 14 times lower overall optical power on the sample.

196 **B. Comparison with compressed sensing.** The accelerated dual-mode imaging protocol exploits the ability to simultaneously sample in
197 real- and k-space in order to achieve acquisition acceleration and power reduction. The protocol shares some similarities with compressed
198 sensing (CS) but differs in other aspects. As summarized in Table S2, we compare these two methods in terms of the following perspectives:

	CS (4, 5)	Dual-mode protocol
Operating regime	A known space is sparse	Real-space is sparse
Principle	RIP and ℓ_1 minimization	Reciprocity between k- and real-spaces
Technique type	Computational	Physical
Subsampling space	K-space	Both k- and real- spaces
Acceleration	n/m (where $m = \mathcal{O}((k\log(n/k))$ or $\mathcal{O}\left((k\log(n)^4\right), k = 1 - s$)[1]	$\mathcal{O}(1-s)^{1/2}$
Acceleration (example)	40 [2]	25 [3]
Image resolution in this paper [4]	$640\mu m$	$40\mu m$

Table S2. Comparison between CS and Dual-mode protocol. In comparison to MRI CS, the ability to sample simultaneously in 2 spaces provides a new venue to acquisition speedup with additional benefit of resolution improvement. In the table, n, m, s represent image dimension, number of measurements, sparsity (the portion of dark pixels) respectively.

199 ***B.1. Compressed sensing.*** Let us first briefly review basics of CS, in order to better compare it with our protocol. CS is the origin of a major
200 evolution in signal processing (4, 5). It is widely applied in photography, medical imaging, as well as astronomy, because of its ability to
201 recover the signal from very few linear measurements.

202 **Operating regime –** CS, when applied in imaging, operates in a regime where a known representation of the target image is sparse.
203 There usually exists a sparse representation (eg. wavelet or finite-difference representation)(6) for a natural image that encodes certain
204 patterns or structures. The sparsity, which is central to CS, makes it possible to compress information in a large dimensional space into fewer
205 measurements.

206 **Principle –** The key principle that makes CS successful in MRI are random measurements satisfying restricted isometry property (RIP)(5)
207 as well as ℓ_1 minimization in a sparse representation reconstructing image space.

208 More specifically, let us describe the general ideas of CS quantitatively while skipping mathematical proofs. Let $\bar{u}$ be the true underlying
209 image of interest and $\Psi \in \mathbb{C}^{m \times n}$ ($m < n$) be a sensing (sampling) matrix, where m is the number ocan RIP conditionf measurements, and n
210 is the dimension of the image vector that represents a collection of image pixels. An encoding process employs a certain physical means to
211 collect data $b \in \mathbb{C}^m$ that is $\Psi\bar{u}$. A decoding process is used to reconstruct the image $\bar{u}$ from b.

212 We suppose that signal $\bar{u}$ is sparse in representation Φ, namely $\Phi\bar{u}$ is a sparse vector. To reconstruct $\bar{u}$, one normally solves the ℓ_1 problem
213 when there is no noise:

$$\ell_1 : \min_u \{\|\Phi u\|_1 : \Psi u = b\} \tag{11}$$

215 If a measurement matrix $A = \Psi\Phi^\dagger$ satisfies the restricted isometry property (RIP) condition, which indicates A preserves the Euclidean
216 2-norm of S-sparse vectors, the reconstruction has a high probability to yield the true image $\bar{u}$. One of the most known cases that could make
217 A satisfy this condition is CS MRI where one collects under-sampled k-space data and minimizes ℓ_1 norm in wavelet or finite different space.
218 In summary, measured data b with m entries reconstructs u which has n elements.

219 **Acceleration –** CS allows a factor of n/m acceleration in comparison with sampling n points in full. The minimum number of
220 measurements for successful reconstruction is $m = O((1-s)\log(n/(1-s)))$ and $O\left((1-s)\log(n)^4\right)$, when Ψ is a Gaussian random
221 matrix and partial Fourier ensemble respectively. Practically one finds that only when $m \sim > 5(1-s)$, can the RIP condition be satisfied
222 and a reasonably good-quality image can be reconstructed. As a result, the acceleration factor is $\sim \frac{1}{5(1-s)}$. In order to compare CS with our
223 dual-mode accelerated protocol, we assume there is a case where real-space is considered to be the sparse space, and $(1-s) = 0.5\%$. This
224 gives us an acceleration factor of 40.

225 **Image resolution –** In the case of CS MRI, the image resolution is ultimately determined by the k-space sampling window, which is similar
226 to a conventional MR image. The MRI spatial resolution is given by:

$$\delta x \propto \frac{1}{\gamma G_{max}\tau} \tag{12}$$

228 where γ is gyro-magnetic ratio, G_{max} is maximum imaging gradient, and τ is echo time.

229 **Technical challenges –** CS in MRI is mainly a algorithmic technique that is usually easy to implement as long as one has the ability to
230 randomly sample k-space. The major challenge however emerges when the image dimension n is large, for instance 3D imaging, and large
231 computational power is required to solve the convex optimization problem.

Xudong Lv, Jeffrey H. Walton, Emanuel Druga, Fei Wang, Alessandra Aguilar, Tommy McKnelly, Raffi Nazaryan, Fanglin Linda Liu, Lan Wu, Olga Shenderova, Daniel B. Vigneron, Carlos A. Meriles, Jeffrey A. Reimer, Alexander Pines

B.2. Accelerated dual-mode protocol. The accelerated dual-mode protocol proposed in this work takes sub-sampled k-space data by MR as a reference to guide real-space measurement by optics. This protocol warrants acquisition time saving concurrently with optical power reduction.

Operating regime – Such protocol normally presents speedups in the cases where an image is sparse in real-space. In most of the diamond particle imaging, such as tracking or targeting, the criterion is satisfied because diamonds occupy few pixels in a large FOV when we consider such applications. We note that, the preliminary image is "generated" during the process rather than "required" as a precondition of our protocol. Thus, while we consider optical imaging and MRI together as a complete unit, the requirement for an image that is suitable for our dual-mode protocol is only real-space sparsity.

Principle – The principle of the protocol is the reciprocity of the real- and k-spaces, where optical and MR imaging take place respectively. The fact that very few k-space points can lead to a coarse real-space model stems from the Fourier reciprocity. Such principle thus differs from CS. The divergency of the principles of CS and the dual-mode protocol may allow us to superimpose the two methods to get benefits from both. Specifically, random sampling together with convex minimization reconstruction can provide a blurry real-space image for optical real-space imaging to refine. Although the idea is straightforward, it requires careful design of the protocol and the reconstruction algorithm. More details will be in a forthcoming manuscript.

Acceleration – The acquisition can be accelerated by a factor proportional to $(1-s)^{1/2}$. If we take $(1-s) = 0.5\%$ as an example, imaging acceleration is 25 (see main Figure 4C). Notably, additional imaging power reduction happens concurrently with acceleration due to having less pixels necessary for optical excitation.

Image resolution – In contrast to CS, the resolution of the image reconstructed by the protocol is determined by optical resolution. As analyzed in the Section D., for a mm-deep buried sample, image resolution δx can be approximated to proportional to d (Fig. S3) as $\delta x \propto d$ by integrating the Wigner function assuming the scattering media is homogeneous. The ultimate resolution limit of optical imaging at $d = 0$ is set by the diffraction limit $\delta x = \frac{\lambda}{2} \sim 0.3 \mu m$, where λ is the wavelength of the fluorescent light.

Technical challenges – The method is an experimental approach compared to CS which is mainly algorithmic. The protocol relies on acquiring information in k-space first and feedforward it to real space sampling. Thus, the protocol yet requires implementation of a scanning optical imaging platform in addition to MR imaging facilities. Optical setups are normally easy to build at lower cost though.

B.3. Similarities. Apart from the differences described above, CS and dual-mode accelerated protocol share some similarities in the following ways.

Subsampling – Both methods exploit subsampling to avoid scanning across the entire imaging space and therefore gain time saving. CS MRI subsamples k-space while our protocol subsamples both Fourier conjugate spaces.

Sparsity – Both methods rely on sparsity, which is the key to data compression in general. Sparsity means that when a signal is represented in a certain basis, eg. $I = \sum a_i \phi_i$, the majority of the coefficients a_i are 0. This indicates that the number of linearly independent coefficients is less than the dimension of the image-space. Both CS and our protocol take advantage of the sparsity of the target image to compress the number of samples and achieve imaging acceleration.

3. Imaging efficiency of two modalities

In this section, we estimate and compare the imaging efficiency of the optical and MR modalities. We assume the imaging objects are randomly oriented diamond particles buried under depth of d in certain media. Green incident photons pass through the media to excite the diamonds, while either an optical detector and or an MRI detector (RF coil) are utilized to image the particles.

A. Imaging efficiency of optics. To unravel more clearly the factors that affect imaging efficiency, we consider the overall "*signal path*" from the green photon excitation to the ultimate collection of red fluorescence.

1. Green photon scattering and loss at media. Scattering and attenuation lead to loss of photon flux. The attenuation loss can be evaluated by Beer's law: $\frac{\varphi_p}{\varphi_m} = \exp\{\int_0^{d_0} -[\alpha(d) + \mu(d)] \cdot dd\}$, where φ_p is the photon flux of the incident pump beam, and φ_m is the part that reaches diamonds. $\alpha(d)$ and $\mu(d)$ denote the attenuation and scattering coefficient of the media respectively. A typical attenuation coefficient $\alpha(d)$ for skin tissue is about 2 cm^{-1} at the wavelength of 532nm[7]. The scattering coefficient can be written as $\mu = R \cdot \lambda^{-4}$[8] for Rayleigh scattering. We take scattering coefficient of 13.5 cm^{-1} at 532nm which is calculated based on fatty tissue data in [1]. For diamond buried under 3 mm of such media, we estimate an attenuation loss of 0.54 and scattering loss of 1.7×10^{-2}, and hence $\eta_{o,1} = \frac{\varphi_p}{\varphi_m} = 9.6 \times 10^{-3}$. Note that here we have ignored the losses due to the reflection at the diamond surface, which is on the order of 0.83 at near-normal angles of incidence [9], and can be considered negligible compare to $\eta_{o,1}$.

2. Green-to-red photon conversion. In fact, during optical illumination, only a small portion of the incident green photons finally convert to red photons by NV centers. We now estimate this conversion rate $\eta_{o,2}$ based on Ref [9] . A waveguide is employed on a 0.1 ppm NV diamond crystal in this literature, however, we only take the reported single pass conversion efficiency which is relevant to our experimental scenario. We then have $\eta_{o,2} = 5.5 \times 10^{-5}$.

3. Total internal reflection loss. NV centers emit in red, and a portion of the emission light can be restricted within the diamond because of total internal reflection (TIR). The critical angle of TIR for a diamond-media interface is $\theta_c = \arcsin(n_m/n_d) = 24.6°$. We calculate $\eta_{o,3}$ as the portion of the light that is not confined in diamond at the first incidence. Assuming $n_m = 1$, the high refractive index of diamond ($n_d = 2.4$) leads $\eta_{o,3} \approx 9 \times 10^{-2}$ [10].

4. Red fluorescence loss. Optical imaging incurs "*round-trip*" losses due to the need to also collect NV fluorescence. Similar to Step 1 above, one can estimate these attenuation and scattering losses. We take the attenuation coefficient at 650nm as ~ 1 cm^{-1}, and the scattering coefficient as ~ 12.1cm^{-1} (calculated based on fatty tissue data in [1]). For diamonds buried 3 mm deep in such media, we calculate $\eta_{o,4} \approx 1.9 \times 10^{-2}$, where attenuation loss is 0.74 and scattering loss is 2.6×10^{-2}.

Xudong Lv, Jeffrey H. Walton, Emanuel Druga, Fei Wang, Alessandra Aguilar, Tommy McKnelly, Raffi Nazaryan, Fanglin Linda Liu, Lan Wu, Olga Shenderova, Daniel B. Vigneron, Carlos A. Meriles, Jeffrey A. Reimer, Alexander Pines

289 *5. Geometric effects in light collection.* The finite numerical aperture (NA) of the detection optics restricts the total number of photons that
290 can be collected. Only fluorescence light within a solid angle Ω can be captured by the objective lens. We have:

$$\Omega = 2\pi(1 - \cos(\theta_{max})), \tag{13}$$

292 where $\theta_{max} = \arcsin(\text{NA}/n_d)$. Assuming that the fluorescence emission is initially spatially isotropic, the detection efficiency can be
293 expressed as $\eta_o^5 = \Omega/4\pi$. Considering NA = 0.18 in our experiment, we estimate $\eta_{o,5} = 8 \times 10^{-3}$.

294 *6. Signal amplitude reduction by lock-in detection.* Finally, we consider the amplitude loss caused by lock-in detection in practical scenarios.
295 Lock-in techniques are normally used when optical background presents, and the signal of interest can be discerned by the method. However,
296 such benefit of background suppression comes at the cost of reduced overall signal amplitude. This stems from the finite modulation contrast
297 ($<100\%$) upon application of magnetic fields (see main Figure 2A). Since only the component that can be modulated is recovered, the overall
298 signal is weighted by the modulation contrast ($\sim10\%$ typical in our experiments, as in main Figure. 2A(ii)), $\eta_{o,6} \approx 0.1$.

299 Putting together these factors, we estimate the approximate loss incurred from green photons leaving the light source to finally being
300 detected as florescence. This signal-loss chain already draws a strong contrast of optical imaging with the case of MRI, since in the latter
301 section, MRI circumvents scattering losses on the return path. In summary, for the example case of of diamond particles imaging under 3 mm,

302 $\eta_o = \prod_{i=1}^{6} \eta_{o,i} = 7.2 \times 10^{-13}.$

303 **B. Imaging efficiency of MRI.** We now perform a similar analysis for the case of MR imaging. While there is indeed less loss in MRI
304 compared to the "round-trip" loss of optics, there are additional factors related to the inductive detection of the ^{13}C magnetization. Once again
305 we ignore the efficiency of the NMR detector itself (related to preamplifier gain and noise) and focus instead only on the signal chain up to the
306 detector.

307 *1. Green laser loss at media.* Similar to the optical imaging case, since the hyperpolarization is optically induced, we continue to incur
308 *one-way* optical scattering and attenuation losses through the imaging media, corresponding to a factor $\eta_{m,1} = \eta_{o,1} = 9.6 \times 10^{-3}$ as above.
309 *2. Quantum efficiency of ^{13}C hyperpolarization.* Let us now estimate efficiency of the ^{13}C hyperpolarization process. In Figure 1C, the
310 hyperpolarization signal is obtained by 1W laser irradiation with a duration of 40s; as a result, the 10mg natural abundance diamond sample
311 is polarized to $\sim0.3\%$. The number of polarized ^{13}C spins n_c can be calculated as $n_c = \frac{m}{MW} \cdot P \cdot \epsilon \cdot N_A$, where m, MW, P, ϵ, N_A are:
312 the mass of the diamond powder, the molecular weight of the sample, ^{13}C polarization, ^{13}C enrichment and Avogadro number. We obtain
313 $n_c = 5.0 \times 10^{16}$. On the other hand, the total number of green photons used to pump the diamond is:

$$n_p = \frac{1W \times 40s}{\hbar \times \frac{3 \times 10^8 \text{m/s}}{532 \text{nm}}} = 1.1 \times 10^{20} \tag{14}$$

315 leading to a total efficiency $\eta_{m,2} = \frac{n_c}{n_p} = 1.4 \times 10^{-4}$. This also indicates that approximately 7200 green photons can effectively polarize one
316 ^{13}C nuclear spin. We note here: our experiments suggest that when a sample is ^{13}C enriched to 10%, the overall polarization enhances 10
317 times. This result implies that the efficiency can be further boosted by at least an order of a magnitude with ^{13}C enrichment.

318 *3. Geometric factors related to detection.* The sample filling factor in MR imaging plays a similar role as the geometric factors related to
319 finite numerical aperture in optical imaging. In our experiments, the volume of the coil is approximately 2400 mm^3, and the typical volume
320 occupied by the particles is 11 mm^3, implying a relatively low filling factor of $\eta_f = 4 \times 10^{-3}$. The MR signal scales $\propto \eta_f^{1/2}$ when the volume
321 of the coil is fixed (11). We define $\eta_{m,3} = \eta_f^{1/2}$, and we have $\eta_{m,3} = 6.3 \times 10^{-2}$. We note therefore that our filling factor is far from optimal,
322 and can be boosted by at least an order of magnitude by using a coil that is more suitably matched to the sample of interest, or through of use
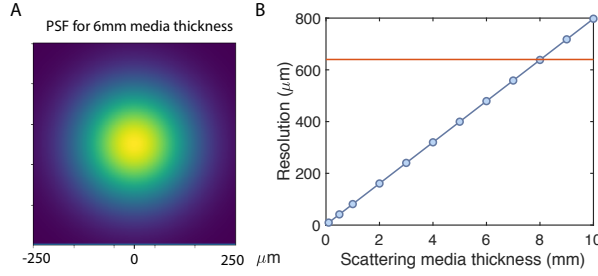323 of inductive coupling coil chains (12).

324 *4. Detection frequency.* We note that the hyperpolarization process delivers ^{13}C polarization that is agnostic to detection field. However, the
325 choice of detection field does play a role in determining the final obtained SNR, scaling as $\propto (Q\omega_0)^{1/2}$ (13), where Q is the quality factor of
326 the coil, and ω_0 is the Larmor frequency under that field.

327 *5.Detection Time.* Finally, the image SNR is also a function of the total effective ^{13}C T_2 coherence time that ultimately bounds the period
328 over which signal can be acquired. While the native T_2^* time is relatively short $\approx$1ms, control techniques that can prolong the coherence time
329 to T_2 or $T_{1\rho}$ can substantially boost image SNR. We will explore these aspects in a forthcoming manuscript.

330 Although making further comparison between both optical and MR modalities requires detailed consideration of the quantum efficiency and
331 amplifier noise in both detectors, the discussion above already demonstrates that both modalities generally have complimentary advantages and
332 are hence are highly amenable to combination. Considering photon losses alone, MR imaging provides a distinct advantage when compared

333 to optical imaging: $\eta_m = \prod_{i=1}^{3} \eta_{m,i} = 8.5 \times 10^{-8}$. This highlights that MR offers advantages for imaging particles that are buried under a

334 scattering media.

335 **C. Estimation of imaging SNR in scattering media.** We compare the *relative* image SNR for optical and MR imaging modalities in
336 scattering media. Defining the ratio of the two SNRs, $\gamma(d)$, where d is the depth of the diamond particles. In our experiments (in the absence
337 of tissue), $\gamma_0 \equiv \gamma(0) = \frac{\text{SNR}_{\text{optical}}}{\text{SNR}_{\text{MRI}}} = 15$. If however, the particles are embedded in a scattering media with a depth of d_0, we expect an
338 additional loss by a factor of $\exp\{\int_0^{d_0} -[\alpha(d) + \mu(d)] \cdot dd\}$ in optical imaging. At a critical depth $d_c = \frac{\log \gamma(0)}{\alpha_0 + \mu_0}$, the optical and MR image
339 SNR become equal ($\gamma(d_c) = 1$). This suggests that MR modality will produce better SNR for objects are beneath d_c. Taking the attenuation
340 and scattering coefficient used in Table S1 , we have $d_c = 2.2$ mm.

Xudong Lv, Jeffrey H. Walton, Emanuel Druga, Fei Wang, Alessandra Aguilar, Tommy McKnelly, Raffi Nazaryan, Fanglin Linda Liu, Lan Wu, Olga Shenderova, Daniel B. Vigneron, Carlos A. Meriles, Jeffrey A. Reimer, Alexander Pines

Fig. S3. Image resolution in scattering media. (A) Simulated wide-field PSF when the point source is scattered by a 6mm-thick media. (B) Relation between resolution and scattering media thickness. Blue dots denote the optical resolution. Red line denotes the MRI resolution corresponding to our experiments.

D. Estimation of imaging resolution in scattering media. Besides SNR reduction, scattering blurs optical images as well, causing resolution reduction. In contrast, MR images are immune to optical scattering, with a resolution primarily being set by gradient strength and coherence time. Indeed, while optical imaging can easily achieve $\sim 1\mu m$ resolution, its performance degrades rapidly with increasing thickness of the scattering media. To illustrate this, we use multi-slice model (14) to simulate the blur of a point source beneath a certain thickness of scattering media. We use a Wigner function $W(\vec{r}, \vec{u})$ to represent the 4D light field, where $\vec{r} = (x, y)$ is the spatial coordinates, and $\vec{u} = (u_x, u_y)$ is the spatial frequency coordinates which is related to the propagation angle θ through $\sin(\vec{\theta}) = \lambda\vec{u}/n_r$. By assuming the scattering media is homogeneous and the spreading of angle $\vec{\theta}$ is Gaussian distributed, Wigner function $W(\vec{r}, \vec{u})$ of the output field can be derived by summing up the propagation and scattering effect from each slice. Propagating through each slice has a tilting effect on $\vec{r}$ and the scattering due to each slice provides a Gaussian blur to $\vec{u}$ (15). Integrating over the frequency coordinates $\vec{u}$ to simulate the measured intensity of a wide-field microscope focusing at a point source through a scattering media of thickness t, we obtain,

$$
\begin{aligned}
I(\vec{r}) &= \iint d^2\vec{u}\, W(\vec{r}, \vec{u}) \\
&= \iint_{(\frac{-n_r\theta}{\lambda}, \frac{-n_r\theta}{\lambda})}^{(\frac{n_r\theta}{\lambda}, \frac{n_r\theta}{\lambda})} d^2\vec{u}\, \frac{n_r^2}{2\pi\lambda^2 t^2\sigma^2}\cdot \\
&\quad \exp\left[\frac{n_r^2}{2\lambda^2 t^2\sigma^2}\left(\vec{r} - \frac{\lambda t}{n_r}\vec{u}\right)^2\right]
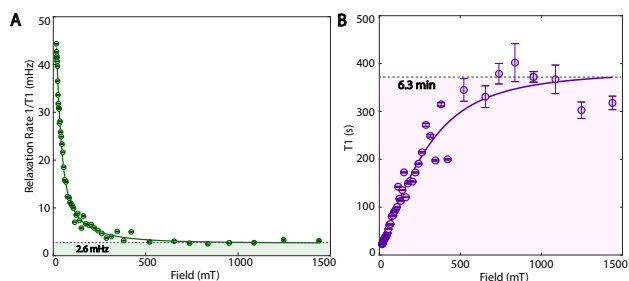\end{aligned}
\tag{15}
$$

The Gaussian standard deviation σ here quantifies the level of scattering. As an illustration in Fig. S3 we employ a typical value $\sigma = 0.052$ corresponding to somatosensory cortex of a mouse brain (16). Assuming $\theta = 0.2527$ rad representing angle of the acceptance of a 0.25 NA objective, we calculate the FWHM of the blurred point spread function as resolution and plot the resolution versus media thickness in Fig. S3B. Since we use homogeneous tissue assumption and σ stays constant, we expect an approximately linear relationship between the blurriness and media thickness. Clearly, optical resolution is superior at shallow depths but MRI can outperform it when the tissue is more than ~ 10 mm thick (Fig. S3B). This results from comparison of the simulated optical resolution with the MRI resolution obtained in our experiments.

4. Materials

A. Diamond particles. The microcrystalline diamond powder involved in experiments in main Figure 1 has ~ 40 mg mass and ~ 200 μm size. The particles enriched with ~ 1 ppm NV centers are from Element6, fabricated by high pressure high temperature (HPHT) growth. We emphasize that while these somewhat large particles were employed as a proof of concept demonstration, dual-mode imaging is currently viable even on smaller diamond nanoparticles. In fact, we have obtained hyperpolarization enhancements of $\lesssim 10$ over 7T on commercially available (Adamas) 100nm fluorescent nanodiamonds (17). The enhancement is limited primarily by material degradation stemming from radiation damage due to high fluence electrons employed to create the vacancy centers, as well as mechanical stresses incurred upon sample crushing. Recent work in (18) has shown that annealing the diamond samples at ultra-high temperatures ~ 1750 °C can largely relieve this radiation-induced lattice disorder and enhance hyperpolarization levels by about an order of magnitude. These material advances along with the use of ^{13}C enrichment portend signal gains that can allow translation of dual-mode imaging to nanodiamonds.

B. T_1 relaxation in diamond. The several minute long ^{13}C T_1 times of the diamond particles present advantages when they are employed as imaging agents (20). In several respects the long T_1 times here are analogous to the long spin lifetimes of ^{29}Si spins in silicon nanoparticles(21) that made the latter systems highly attractive as MR imaging agents. In contrast to hyperpolarized silicon however, optically induced ^{13}C hyperpolarization in diamond is replenishable and generated at room temperature and with much higher throughput.

We comment that the T_1 process in defect-center rich diamond particles primarily proceeds due to interaction of the ^{13}C spins with lattice paramagnetic impurities. Ref. (19) has a detailed exposition on this subject, but for clarity we show in Fig. S4 the field dependence of the ^{13}C T_1 relaxation times of the particles here. In particular, the data illustrates sharp field-dependent relaxation profiles (see Fig. S4A) where the T_1 time drops sharply at low field. Intuitive understanding of the sharp profile is: the ^{13}C Larmor frequency lies within the linewidth of the paramagnetic defect ESR spectrum (primarily P1 centers and radiation induced paramagnetic defects), engendering many-body flip-flops that can act as nuclear polarization relaxation channels. Fortunately however, the T_1 increases and saturates to multiple-minute long values beyond a modest a knee field ~ 100mT. T_1 at this field is long enough to allow for simple polarization retention in permanent magnets.

Xudong Lv, Jeffrey H. Walton, Emanuel Druga, Fei Wang, Alessandra Aguilar, Tommy McKnelly, Raffi Nazaryan, Fanglin Linda Liu, Lan Wu, Olga Shenderova, Daniel B. Vigneron, Carlos A. Meriles, Jeffrey A. Reimer, Alexander Pines

Fig. S4. T_1 **lifetimes of** ^{13}**C nuclei**, measured with 200μm diamond particles employed in this work. (A)^{13}C relaxation rate ($R_1(B) = 1/T_1$) mapped as a function of magnetic field, showing a sharp increase below ∼100mT. Solid line is a Lorentzian fit and error bars are calculated from mono-exponential fits (see (19)). (B) Corresponding relaxation times T_1, emphasizing that long relaxation times (>6 min) are easily achievable even at modest fields.

C. Hyperpolarization in ^{13}**C enriched diamond.** ^{13}C enrichment provides a simple means to increase the effective number of ^{13}C spins in the lattice at fixed sample volumes, and thus potentially increase MR image SNR. In single-crystal diamond samples produced by chemical vapor deposition (cvd) with controlled concentrations of ^{13}C methane, we observe that the hyperpolarization enhancements per ^{13}C nucleus can be approximately maintained to the same level up to an enrichment of about 10% (19). If translatable to diamond particles, this could allow increase of DNP signal by a factor of ∼10 (time savings of ∼100). We also observe a concomitant decrease in the T_1 relaxation times (and polarization buildup times) at higher enrichment (19). Overall these results point to order of magnitude SNR gains if HPHT based particulate diamond materials can be fabricated with high lattice ^{13}C enrichment homogeneity. Efforts in this direction are underway in our laboratory.

D. Biocompatibility. Our focus of this work is to highlight the potential for dual-mode optical and MR imaging brought upon by optically hyperpolarizable agents. While NV centers in nanodiamonds are still the prototypical system of this class, there has been a recent spurt of activity of molecular systems with rare-earth or transition metal ions that share the same properties. Toxicity considerations remain an important consideration for all biomedical applications of such materials, but our goal was to highlight methodological advantages that might arise through the use of optical and MR modes, either simultaneously or in consort with each other. Here we provide a brief summary regarding biocompatibility of nanodiamonds.

Diamond material is inert and chemically stable, and such properties could prevent its reaction inside body. Based on summarizing extensive toxicity studies in Table 2 in Ref. (22), Turcheniuk *et al.* have drawn a general conclusion that nanodiamond derivatives of different origin and sizes do not have damages on basic functions of cells, organs, and animals in a reasonable range of concentrations.

More specifically, low *in-vitro* cytotoxicity has been shown in a couple of studies. For example, the toxicity of nanodiamonds was measured on human lung A549 epithelial cells and HFL-1 normal fibroblasts. The results showed that carboxyl-modified nanodiamonds with a particle size of 5 nm and 100 nm did not reduce the cell viability or affect the protein expression at the concentration of 0.1-100 μg/ml, (23).

In-vivo toxicity studies also found no significant impact of nanodiamonds on animal health (24). The pulmonary toxicity of the nanodiamonds was studied in experiments where they are administered in mice through intratracheal instillation. The work found no noticeable adverse effects in the lungs from the nanodiamonds within the period according to the histopathological and ultrastructural investigations. The results also indicated that nanodiamonds can be extruded through engulfment by lung macrophages. From the studies, we can see that the respiratory toxicity of nanodiamonds, in a wide variety of dose range, is less than that of CNTs and other carbon nanomaterials that are extensively studied in the previous literature (25, 26).

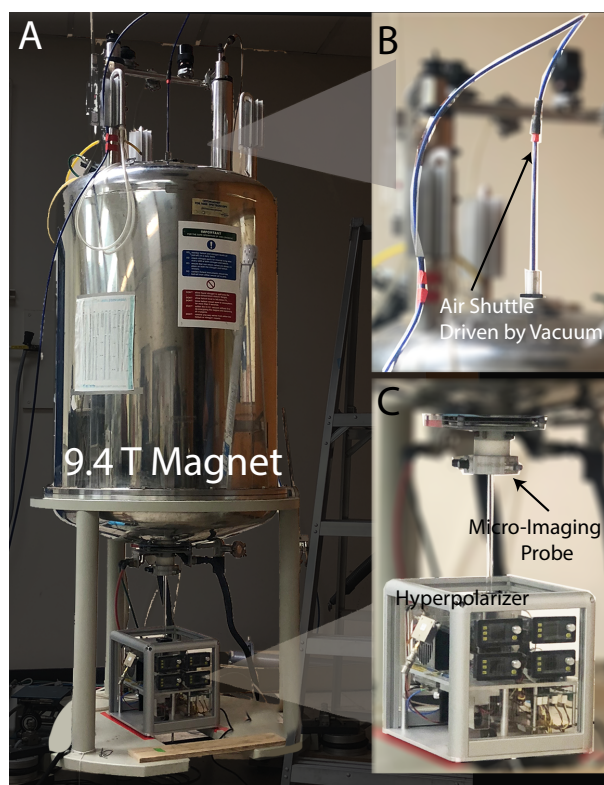Long term studies have been done by replacing water in the mice's diet with nanodiamond hydrosols for 3 to 6 months (27). Neither death nor abnormal in growth or the internal organ (liver, lungs, heart, kidneys, and pancreas) caused by nanodiamonds was found in the results comparing with the control mice indicated. The same study has also shown that there are no effects on the mouse's reproductive ability. No inflammatory symptoms in the mice has been observed after subcutaneous exposure to nanodiamonds for 3 months (28). Furthermore, no immune responses was observed with 10 days after intraperitoneal injection of nanodiamonds (29). It was also found that after filtration to remove large size particles, the uptake of nanodiamonds was significantly reduced in the lung, the spleen and the liver (30). Long period observation (5 month) confirmed no toxicity for dosages as high as 75 mg/kg body weight of nanodiamonds by histopathological analysis of various tissues and organs in mouse models over long period of time (31).

Although diamond nanoparticles tend to remain in body for longer time, it has been found that in a mouse model, the diamond nanoparticles were excreted through urine (30). Specially, a gradual decrease of concentrations in lung, spleen, and liver was observed, and an increase in bladder by PET imaging of ^{18}F labeled nanodiamonds was shown. And 2 hours after administration of nanodiamonds in rats, higher concentration was found in urine than organs.

Given the low toxicity results in both *in-vitro* and *in-vivo* studies as well as the elimination pathway through urine, nanodiamonds have been proposed for cancer therapy, drug delivery, antimicrobial agents as well as biomedical imaging. For example, diamond as a drug delivery carrier has been reported in tissue level (32, 33) and mouse models (34). The diamond-amoxicillin complex in Gutta percha matrix is now in clinical trial as a root canal tooth implant (35).

5. Methods

A. ^{13}**C Hyperpolarized MRI experimental setup.** We now detail the setup employed for diamond hyperpolarization and ^{13}C MR imaging (Fig. S5A). It consists of a pneumatic field-cycling device, a wide-bore 9.4T superconducting magnet, and a miniaturized hyperpolarizer

Xiaojing Lv, Jeffrey H. Walton, Emanuel Druga, Fei Wang, Alessandra Aguilar, Tommy McKnelly, Raffi Nazaryan, Fanglin Linda Liu, Lan Wu, Olga Shenderova, Daniel B. Vigneron, Carlos A. Meriles, Jeffrey A. Reimer, Alexander Pines

Fig. S5. Hyperpolarization experiment setup consists of (A) a 400MHz (9.4T) Bruker DRX system fitted with a micro-imaging probe (10 mm ^{1}H/^{13}C volume coil) for MRI acquisition, and (B) an air shuttle based field-cycling system that transports the sample from low to high field. (C) Polarization is generated in a portable polarizer device placed at the bottom of the magnet.
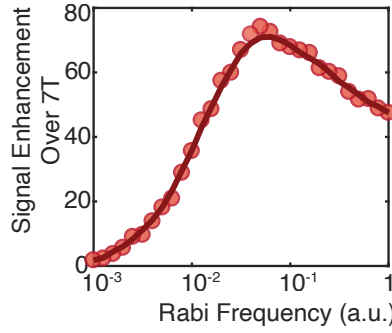
(Hypercube, (17)). The field-cycling device (Fig. S5B) enables rapid sample transfer from low field (40 mT) to the 9.4 T detection field, within which a 10 mm ^{1}H/^{13}C volume coil is installed (Fig. S5C). It is composed of a quartz channel in which the sample is transported, a concave-shaped stopper at the bottom end of the channel, and is driven by a pump that generates the requisite vacuum to drive the transfer. The overall transport time into the magnet is under 1s, short compared to the ^{13}C T_1 times. MR imaging was conducted with a Bruker DRX system and custom programmed 'FLASH' pulse sequence.

The device (Fig. S5C) delivering hyperpolarized diamond particles is small in size ($\sim$25 cm edge) compared to traditional DNP apparatuses (see Ref. (17) for a detailed description). The self-contained unit encapsulates components for laser excitation, and MW irradiation as well as an electromagnet for field fine-tuning. We employ a a 1W 520nm diode laser (Lasertack PD-01289) and passes through an aspheric lens and a set of anamorphic prisms to form a 4 mm diameter beam. The beam was routed by two mirrors to illuminate the sample from the bottom. MW irradiation that drives polarization transfer is generated by three voltage controlled oscillator (VCO) sources (Minicircuits ZX95-3800A+). For frequency sweeps, the VCOs are driven by phase shifted triangle waves from a home-built PIC microprocessor (PIC30F2020) driven quad ramp generator. A typical sweep frequency at 200Hz, approximately determined by the NV T_{1e} lifetime (17), is used to sweep through NV powder spectrum. The on board Hall probes measure the vector magnetic field experienced by the diamond particles, and an algorithm that determines the position of the extrema of the NV powder pattern to sweep over. The VCO signals are then power combined and amplified by a 16 W amplifier, and delivered with a loop antenna. The broadband antenna has substantial reflection and consequent power loss, which we estimate to be greater than 90%. We typically employ a polarizing field $\sim$38 mT, where hyperpolarization enhancements are optimal (17).

B. Evaluation of SAR and optical power. In order to characterize the MW induced heating in potential future deployment of hyperpolarization in in-vivo settings, we detail the evaluation of the Specific Absorption Rate (SAR) (36) with parameters in our experiments. We suppose the MW field implemented is B_1, causing heat generation. Considering this field applied in a cylindrical space between two split coils, we derive the eddy current and the heat generated by the current and obtain:

$$\text{SAR} = \frac{\sigma \pi^2 f^2 B_1^2 D^2}{8\rho} , \qquad [16]$$

where σ and ρ are respectively the conductivity and density of the media; σ =0.57 S/M(37) and ρ =1079 kg/m^3 for human tissue. Assuming $f \approx 2.9$ GHz is the MW frequency, and D =14 mm is the diameter of the split coil, we obtain a SAR = $1.1 \times 10^{12} B_1^2$ W/(kg·T^2) or $1.1 \times 10^4 B_1^2$ W/(kg·G^2) as a function of the B_1 field employed. A direct measure of the electron Rabi frequency is somewhat challenging in our setup, due to MW field inhomogeneity and specifics of the MW delivery platform employed. However we can provide an estimate from a theoretical evaluation of the Landau-Zener hyperpolarization mechanism. Using the estimated $\Omega \lesssim$200 kHz(38), We calculate a SAR of $\sim$14 W/kg. The heating issue needs to be addressed while maintaining enough signal. We note importantly that the hyperpolarization enhancements

Xudong Lv, Jeffrey H. Walton, Emanuel Druga, Fei Wang, Alessandra Aguilar, Tommy McKnelly, Raffi Nazaryan, Fanglin Liu, Lan Wu, Olga Shenderova, Daniel B. Vigneron, Carlos A. Meriles, Jeffrey A. Reimer, Alexander Pines

Fig. S6. Hyperpolarization signal as a function of Rabi frequency. (Data in (39)) Hyperpolarization signal shows approximately logarithmical dependence on Rabi frequency when MW power is smaller than a threshold.
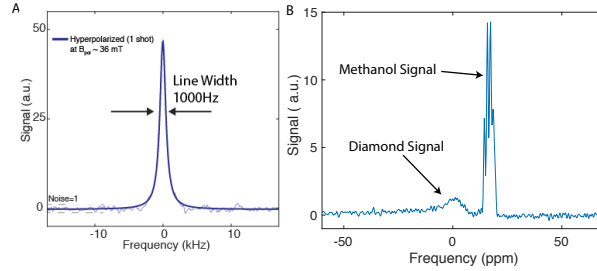
Fig. S7. ^{13}C **NMR spectrum** of diamond and diamond/methanol mixture relevant to the MR background suppression experiments in Figure. 3 of the main paper. (A) Typical hyperpolarized ^{13}C spectrum of diamond with line width $\approx$1kHz (data from (17)). (B) Diamond particles hyperpolarized in a ^{13}C methanol mixture, showing that the two spectra overlap with each other. Note that the in the MR imaging sequences, the pulse bandwidth is 213kHz, and sampling bandwidth is 900 kHz, which are inadequate to distinguish the two sources.

fall approximately logarithmic with MW power beyond a threshold (39), and we can have SNR $\propto \log(B_1)$ from data shown in Fig. S6. In such regime, the relationship between SAR and SNR is: SAR $\propto B_1^2 \propto \exp(2\text{SNR})$. This indicates that it is possible to reduce the SAR by lowering the MW power with a benign loss in the hyperpolarization signal ($\sim$47 % loss) to reach an FDA SAR limit (4 W/kg). Potential SNR improvement through better engineered materials or higher filling factors can compensate such loss and allow further SAR reduction.

Let us comment on optical power as well. The MRI demonstrated in main Figure 1F employed a laser power density of $\sim$80 mW/mm^2. While this is elevated above levels suitable for in-vivo operation ($\sim$4.7 mW/mm^2 (40)), this is primarily on account of the large mass ($\sim$40 mg) of the particles in this experiment. We anticipate that laser power will not be restrictive in preclinical imaging settings since far lower diamond masses are typically employed in the relevant applications.

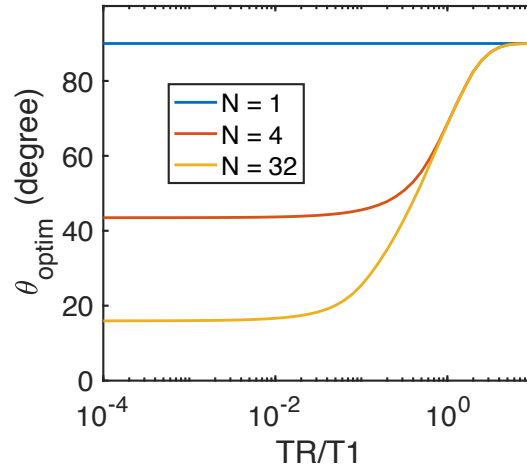**C. Magnetic resonance imaging.** We now consider details of methodology employed to produce the MR images in Figure. 1F of the main paper. The short $T_2^\star \sim$1 ms of the diamond ^{13}C nuclei (see Fig. S7A), as typical in any solid state system (41), present technical challenges for MR imaging. We optimize our gradient echo imaging pulse sequences (see Fig. S9) to account for fast spin dephasing. Specifically, the width of RF pulses and gradient lobes are minimized to create as short an echo time as possible (TE = 0.5 ms), and fast gradient switching (200 μs) is employed for phase encoding. Moreover, since we are only interested here in 2D projection images, the slice selection gradient G_{slice} was removed in our variant of FLASH. This removes transient interference with the subsequent phase encoding gradient and reduces distortions during the short RF pulse. Gradient spoilers were employed on both the phase encoding and readout channels at the end of the sequence to destroy the residual spin coherence and has minimal impact on the subsequent pulse cycle. Finally, taking advantage of the substantial initial polarization, we use small flip angles (θ in Fig. S9) to optimally retain polarization over the entire imaging sequence, distributing the magnetization in each of the phase encoding steps in the most efficient manner.

We now analyze the optimal flip angle employed for imaging. Due to the limitation of the instrumentation, we can only have a constant flip angle θ in all the repetitions. If M_n represents the total magnetization at the beginning of the nth repetition of the imaging sequence, and M_0 represents the thermal magnetization, we can compute a recursive relationship between M_n and M_{n-1}, as well as the transverse magnetization $M_{x,n}$ as :

$$\begin{cases} M_n = (M_{n-1}\cos\theta - M_0)\, e^{-\frac{\text{TR}}{T_1}} + M_0 \\ M_{x,n} = M_n \sin\theta \end{cases} \qquad [17]$$

where TR is the repetition time, and θ the flip angle used to generate transverse magnetization. We consider the cumulative transverse magnetization $S_{\text{cumulative}} = \sum_{n=1}^{N} M_{x,n}$. Assuming that $M_1 \gg M_0$ is self-evident under hyperpolarization, we can optimize θ to maximize $S_{\text{cumulative}}$ (see Fig. S8). For a total of $N =$32 repetitions, $\theta_{\text{optim}} =$15° corresponding to a 6μs pulse width under 2dB RF attenuation.

The imaging sequence implemented in our experiments is detailed in Fig. S9. We employed hard pulses with bandwidth 213kHz, which is sufficient to cover the entire ^{13}C spectrum. The small flip angle sequence is repeated 32 times to obtain 32 lines in phase encoding dimension,

Xudong Lv, Jeffrey H. Walton, Emanuel Druga, Fei Wang, Alessandra Aguilar, Tommy McKnelly, Raffi Nazaryan, Fanglin Linda Liu, Lan Wu, Olga Shenderova, Daniel B. Vigneron, Carlos A. Meriles, Jeffrey A. Reimer, Alexander Pines

Fig. S8. Optimization of flip angle θ employed for MR imaging. Here we consider simulated traces for the case of image consisting of N = 1, 4, 32 slices, and plot the flip angle θ_{opt} that maximizes the total transverse magnetization $S_{\text{cumulative}}$ over the entire imaging sequence. Our experiment corresponds to the regime where TR/T1 $\sim 10^{-3}$, indicating the optimal flip angle for $N = 32$ employed in the images in main Figure. 1F is $\sim 15°$.
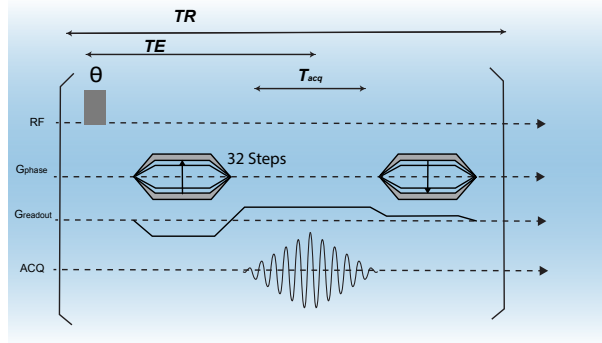
Fig. S9. MR imaging sequence. A variant of FLASH is used in the MRI experiments in this paper. Here echo time TE = 0.5 ms, repetition time TR = 6 ms, acquisition time T_{acq} = 0.36 ms, and we employed 32 phase encoding and 32 frequency encoding steps.
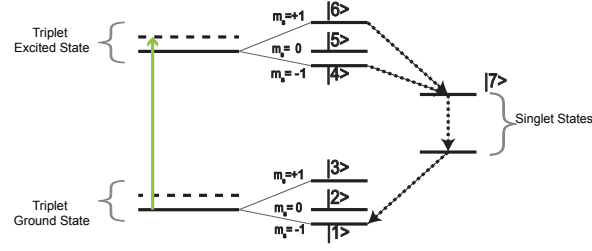
and each phase encoding step includes 32 points in frequency encoding dimension. The sampling dwell time is 0.011ms, giving a sampling bandwidth of $\approx$ 90kHz. Sampling in phase encoding dimension proceeds in a centric fashion, k={$0, -1, +1, \cdots -16$}, so as to place the largest signal at the center of k-space, and a FFT finally produces the MR image. In our experiment, a typical spatial resolution is 0.64 mm $\times 0.64$ mm, which after zero-filling and smoothing results in a square pixel size (main Figure. 1F) of 0.16 mm. We note that since in the absence of slice selection, any image we obtain is a 2D projection along z-axis.

Let us comment on approaches to extend the diamond particle imaging to 3D. The short T_2^* of ^{13}C in diamond that prevents longer acquisition is the major challenge in the cases of 3D imaging. Refocusing sequences such as magic echo sequence (42) or quadratic echo sequence (43) can prolong the coherence time during which imaging takes place. Ultrashort TE, or UTE sequences (44) is another approach where gradient on both phase encoding and frequency encoding dimensions can be applied while the acquisition channel opens right after RF excitation. Such sequences can allow us to either implement slice selection or phase encode the information along the third dimension.

**D. Optical imaging.** We describe the details of optical imaging in this section. Optical imaging of diamond particle fluorescence in Figure. 1E employed four laser-diodes (Lasertack PD- 01289), coupled with optical fibers (Thorlabs M35L01) to uniformly irradiate the sample from four orthogonal directions. Note that, hyperpolarization is conducted with one laser. The fluorescence is filtered by a 630 nm long pass filter (Thorlabs FGL630) before light collection, either by an avalanche photodiode (APD) (Thorlabs APD410) or a CMOS camera (DCC1645C) equipped with an objective lens (MVL5M23). The APD output allows quantification of the overall sample fluorescence, and was recorded by a data acquisition card (NI USB 6229). Such APD data is presented, for instance, in Figure 2A of the main paper. The optical images and time elapsed data for background suppression are instead obtained from the CMOS camera, employing a 10Hz frame rate.

Adding a third dimension to optical imaging may require a confocal-type of setup, and scattering can largely deteriorate the quality of optical images. We envision that the dual-mode imaging capability can overcome the challenge by augmenting the optical images with three dimensional MRI.

E. Photon counts estimation. We estimate the overall photon counts in the optical imaging via the a Thorlabs APD410 photo diode. Without changing the imaging setup, we measured a voltage from the APD $V_{out} = 3$V in front of the camera. Referring to the manual (45), we

Xudong Lv, Jeffrey H. Walton, Emanuel Druga, Fei Wang, Alessandra Aguilar, Tommy McKnelly, Raffi Nazaryan, Fanglin Linda Liu, Lan Wu, Olga Shenderova, Daniel B. Vigneron, Carlos A. Meriles, Jeffrey A. Reimer, Alexander Pines

Fig. S10. NV energy level structure simplified to a 7-level model. The NV- centers are electronic spin-1 with ground and excited triplet states, as well as a "dark" singlet state. The $m_s = \pm 1$ states degenerate at zero field and split into two states when an external magnetic field is applied.
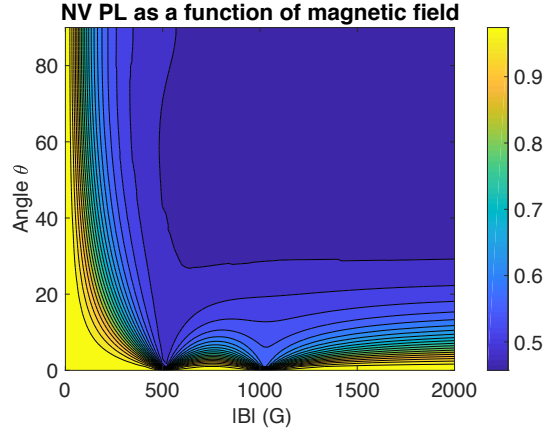
Fig. S11. NV photoluminescence as a function of external magnetic field and the angle between magnetic field and the N-V axis. This is simulated from a 7-energy-level model of NV state kinetics assuming no charge interconversion between NV charge states. Highest contrast appears close to excited and ground state anti-crossing at 500G and 1000G.

500   have responsivity $R_M(637 \text{ nm}) = 33$ A/W, and the corresponding incident light power per volt of electrical output P_{icd}/V_{out}=1.21 $\times 10^{-7}$W/V.

501   We estimate the integrated photon counts in a typical image (main Figure 1E) to be 12×10^{11} counts/s.

502   **F. Optical and MR image SNR estimation.** We now detail methods employed to estimate the image SNRs in the optical and MR images in

503   Figure. 1 E, F of the main paper. We manually select a circular region of interest (ROI) to measure the mean signal value in the "object region",

504   and move the same ROI away from the object to a background region to measure the noise level. The SNR is measured 10 times at different

505   locations on both images, and an average is taken to quantify image SNR. We thus obtain a normalized one-shot SNR of 1.05 for the MR

506   image in Figure. 1F. For optical image (Figure. 1E), the measured SNR is 12.0 in 0.1s of acquisition. In order to draw a fair comparison, we

507   rescale this SNR to 3.0 for the same optical power employed in MRI.

508   We then normalize the SNR against acquisition time. We obtain an optical SNR of $9.5\sqrt{\text{Hz}}$, and MRI of $0.63\sqrt{\text{Hz}}$ (with consideration

509   of 40s dead time to hyperpolarize the sample). We note that MR SNR can be substantially improved beyond this value by several factors,

510   including ^{13}C enrichment, improvements in filling factor, material optimization (18), as well as carefully designed pulse sequence.
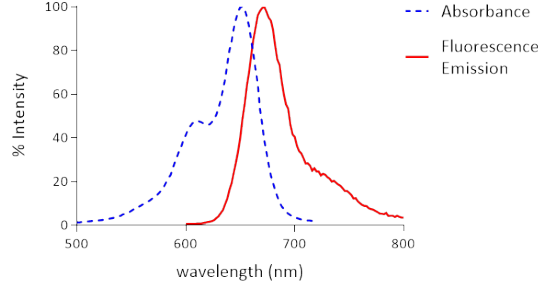
511   **G. Pulsed field fluorescence modulation.** The magnetic field dependence of NV fluorescence enables amplitude modulation of optical

512   images (main Figure 2A, B). We simulate this effect using the method in a pioneering work in Ref. (46) but include a detailed description here

513   for completeness. When an external magnetic field is not perfectly aligned with the N-V axis, it lifts the degeneracy of the $m_s = \pm 1$ levels and

514   mixes the $m_s = \pm 1$ and $m_s = 0$ states. This effect can be simulated a 7-level-model of the NV- center (Fig. S10), where the singlet dark states

515   are considered as one state $|7\rangle$. Upon application of a static magnetic field $\mathbf{B}_{ext}$, the eigenstates $|i\rangle$ of the system can be expressed as linear

516   combinations of the zero-field eigenstates $|i\rangle = \sum_{j=1}^{7} \alpha_{ij}(\mathbf{B}_{ext}) |j^0\rangle$. The ground state and excited state Hamiltonian can be written as:

517
$$\mathcal{H}_{\text{gs}} = hD_{\text{gs}}S_z^2 + g\mu_{\text{B}}\mathbf{B}_{ext} \cdot \mathbf{S}$$
$$\mathcal{H}_{\text{es}} = hD_{\text{es}}S_z^2 + g\mu_{\text{B}}\mathbf{B}_{ext} \cdot \mathbf{S}$$
[18]

518   where D_{gs} and D_{es} are zero field splitting of the ground state and the excited state. We diagonalize the Hamiltonian to estimate $\{\alpha_{ij}(\mathbf{B}_{ext})\}$.

519   Following Ref. (46), the dynamics of population in the different states can be evaluated as:

520
$$\frac{\mathrm{d}n_i}{\mathrm{d}t} = \sum_{j=1}^{7} (k_{ji}n_j - k_{ij}n_i)$$
[19]

Xudong Lv, Jeffrey H. Walton, Emanuel Druga, Fei Wang, Alessandra Aguilar, Tommy McKnelly, Raffi Nazaryan, Fanglin Linda Liu, Lan Wu, Olga Shenderova, Daniel B. Vigneron, Carlos A. Meriles, Jeffrey A. Reimer, Alexander Pines

Fig. S12. Optical spectrum of the Alexa 647 dye as a background employed in the experiments in Figure 3C of the main paper (adapted from datasheet (47)). It is evident that the fluorescence emission of overlaps strongly with NV emission spectrum, making the diamond particles indistinguishable in the background but recoverable through lock-in modulation under a pulsed magnetic field.

where n_i is the population of the $|i\rangle$ state, and k_{ij} denotes the kinetic transition rate between state $|i\rangle$ and $|j\rangle$. The transition rates $\{k_{ij}(\mathbf{B}_{ext})\}$ are associated with the zero-field transition rates $\{k_{pq}^0\}$ through the transformation $k_{ij}(\mathbf{B}_{ext}) = \sum_{p=1}^{7}\sum_{q=1}^{7}|\alpha_{ip}|^2|\alpha_{jq}|^2 k_{pq}^0$. We employ experimentally measured values of $\{k_{pq}^0\}$ from Ref. (46). Solving the steady state of the kinetic equations, we obtain steady state photoluminescence $\mathcal{R}$ as a function of applied $\mathbf{B}_{ext}$:

$$\mathcal{R}(\mathbf{B}_{ext}) = \sum_{i=4}^{6}\sum_{j=1}^{3}k_{ij}(\mathbf{B}_{ext})n_i \tag{20}$$

Evaluating $\mathcal{R}(\mathbf{B}_{ext})$ for different magnetic field strengths and angles with respect to the N-V axis, we plot a fluorescence map in Fig. S11. Considering now a randomly oriented powdered diamond sample with sufficiently high mass such that all the angles θ between $\mathbf{B}_{ext}$ and N-V axis are uniform, the overall fluorescence as a function of applied magnetic field is:

$$D(|\mathbf{B}_{ext})|) = \frac{\int_0^\pi \mathcal{R}(|\mathbf{B}_{ext}|,\theta)\sin(\theta)d\theta}{\int_0^\pi \sin(\theta)d\theta} \tag{21}$$

The result is shown in Figure. 2A of the main paper. We note that while this simple model points to an attainable contrast approaching $\sim$40% for a field strength $\sim$40 mT, we experimentally obtain a lower contrast $\sim$ 10%. We speculate that the discrepancy stems from NV charge state interconversion and light scattering, both of which are not accounted for in this model, and are challenging to estimate with precision in our experimental settings.

H. Dual-mode background suppression. Modulation of the images in both the optical and MR modalities allows effective suppression of background signals. We now provide more details about the experimental demonstration in Figure 3 of the main paper. For the optical images where Alexa 647 overlapping with NV centers on the optical spectrum (Fig. S12) is utilized as an artificial background, we employ software lock-in suppression. In such method, we record a 100s time lapse at 10 fps when modulating the signal of the entire image with a $\approx$400 G amplitude, 0.1 Hz square wave field applied to the sample. Due to the mechanism outlined above, only fluorescence from the diamond particles are modulated by the field change, and a peak at 0.1 Hz will present for these pixels in the Fourier domain, allowing the lock-in reconstructed wide-field background-free image is shown in Figure 3E. Although the images here constitute a proof of concept demonstration and the suppressed background is $\sim$2 times of the signal, the robust and non-blinking modulation from the particles engender background suppression factors that can be as high as 2 orders of magnitude (48).

Common mode rejection is used in ^{13}C MRI for background suppression, exploiting the unique ability of our hyperpolarization method to entirely reverse the ^{13}C polarization on-demand. We chose a background consisting of [^{13}C]-methanol, since its spectrum (shown in Fig. S7B) appears very close to that of ^{13}C in bulk diamond. The background suppressed is $\sim$5 times of the signal in Figure 5D. While this constitutes a proof a concept, we emphasize that the suppression factors can exceed two orders of magnitude (17).

I. Comparison with ^{1}H relaxation contrast imaging. ^{1}H imaging with conventional exogenous contrast agents has been extensively used in MRI studies (49). In our work, we propose to image the nanodiamond object directly in contrast to some contrast imaging techniques relying on imaging the relative difference of relaxation time of the objects. It is different from 1H contrast imaging in two aspects: (i) nuclei species: 13C imaging presents relatively smaller SNR but much lower background than 1H imaging. (ii) contrast mechanism: our hyperpolarization contrast is usually higher than relaxation (T_1 or T_2) contrast.

In order to compare two approaches, we can define a contrast-to-noise ratio (CNR) to quantify the image quality: $\text{CNR} = \frac{\text{signal difference}}{\text{noise}}$. Assuming the signal of the object and background is s_o and s_b respectively, and the noise is n, we can rewrite CNR as:

$$\text{CNR} = \frac{s_o - s_b}{n} = \frac{s_o}{n}\frac{s_o - s_b}{s_0} = \text{SNR}\frac{s_o - s_b}{s_o} \tag{22}$$

Xudong Lv, Jeffrey H. Walton, Emanuel Druga, Fei Wang, Alessandra Aguilar, Tommy McKnelly, Raffi Nazaryan, Fanglin Linda Liu, Lan Wu, Olga Shenderova, Daniel B. Vigneron, Carlos A. Meriles, Jeffrey A. Reimer, Alexander Pines

For the first term, the SNR of ^{1}H imaging is usually higher than ^{13}C imaging given high spin density and high gyromagnetic ratio. For the second term $\frac{s_o - s_b}{s_o}$, our approach of direct ^{13}C imaging can have much larger value than relaxation contrast imaging. In our approach, $\frac{s_o - s_b}{s_o} = \frac{\eta n - n_b}{\eta n}$, where n and n_b are the nuclear spin concentration for the object and the background respectively, and $\eta \approx 300$ is the hyperpolarization enhancement factor. The local spin density where diamond particles situate is much higher than the 1% ^{13}C background, so we can estimate $\frac{n}{n_b} \leq 1$, resulting in $\frac{s_o - s_b}{s_o} \approx 1$. On the other hand, in the case of relaxation contrast imaging, we take the saturation recovery T_1 weighted imaging as an example and $\frac{s_o - s_b}{s_o} = \frac{e^{-\mathrm{TR}/T_1} - e^{-\mathrm{TR}/T_{1b}}}{e^{-\mathrm{TR}/T_1}}$, where TR is the echo time and T_1 and T_{1b} are relaxation time for the object and background. Assuming $T_1 = 0.5$ ms and $T_{1b} = 0.1$ ms, while TR = 5 ms, and this term ~ 0.1, which is smaller than 1 in the case of hyperpolarized ^{13}C imaging.

Combining the two terms in this example, we can conclude that in situations where the SNR of the 1H contrast imaging is less than 10 times of the ^{13}C direct imaging, our approach presents a higher CNR. Similar comparison principle can be extended to more general cases: when the second term in the expression can offset the loss in the SNR term, our approach is better than ^{1}H relaxation-based imaging approaches.

References

1. SL Jacques, Optical properties of biological tissues: a review. *Phys. Medicine & Biol.* **58**, R37 (2013).
2. E Fischer, R Kimmich, N Fatkullin, G Yatsenko, Segment diffusion and flip-flop spin diffusion in entangled polyethyleneoxide melts: A field-gradient nmr diffusometry study. *Phys. Rev. E* **62**, 775 (2000).
3. SK Sarkar, et al., Wide-field in vivo background free imaging by selective magnetic modulation of nanodiamond fluorescence. *Biomed. optics express* **5**, 1190–1202 (2014).
4. EJ Candes, T Tao, Near-optimal signal recovery from random projections: Universal encoding strategies? *IEEE transactions on information theory* **52**, 5406–5425 (2006).
5. DL Donoho, Compressed sensing. *IEEE Transactions on information theory* **52**, 1289–1306 (2006).
6. M Lustig, D Donoho, JM Pauly, Sparse mri: The application of compressed sensing for rapid mr imaging. *Magn. Reson. Medicine: An Off. J. Int. Soc. for Magn. Reson. Medicine* **58**, 1182–1195 (2007).
7. T Lister, PA Wright, PH Chappell, Optical properties of human skin. *J. biomedical optics* **17**, 090901 (2012).
8. SL Jacques, Origins of tissue optical properties in the uva, visible, and nir regions. *OSA TOPS on advances optical imaging photon migration* **2**, 364–369 (1996).
9. H Clevenson, et al., Broadband magnetometry and temperature sensing with a light-trapping diamond waveguide. *Nat. Phys.* **11**, 393 (2015).
10. D Le Sage, et al., Efficient photon detection from color centers in a diamond optical waveguide. *Phys. Rev. B* **85**, 121202 (2012).
11. DI Hoult, R Richards, The signal-to-noise ratio of the nuclear magnetic resonance experiment. *J. Magn. Reson. (1969)* **24**, 71–85 (1976).
12. A Hai, VC Spanoudaki, BB Bartelle, A Jasanoff, Wireless resonant circuits for the minimally invasive sensing of biophysical processes in magnetic resonance imaging. *Nat. biomedical engineering* **3**, 69 (2019).
13. D Hoult, The nmr receiver: a description and analysis of design. *Prog. Nucl. Magn. Reson. Spectrosc.* **12**, 41–77 (1978).
14. AM Maiden, MJ Humphry, J Rodenburg, Ptychographic transmission microscopy in three dimensions using a multi-slice approach. *JOSA A* **29**, 1606–1614 (2012).
15. HY Liu, et al., 3d imaging in volumetric scattering media using phase-space measurements. *Opt. express* **23**, 14461–14471 (2015).
16. NC Pégard, et al., Compressive light-field microscopy for 3d neural activity recording. *Optica* **3**, 517–524 (2016).
17. A Ajoy, et al., Room temperature "optical nanodiamond hyperpolarizer": Physics, design, and operation. *Rev. Sci. Instruments* **91**, 023106 (2020).
18. M Gierth, et al., Enhanced optical 13c hyperpolarization in diamond treated by high-temperature rapid thermal annealing. *Adv. Quantum Technol.* **n/a**, 2000050 (2020).
19. A Ajoy, et al., Hyperpolarized relaxometry based nuclear t 1 noise spectroscopy in diamond. *Nat. communications* **10**, 1–12 (2019).
20. E Rej, T Gaebel, T Boele, DE Waddington, DJ Reilly, Hyperpolarized nanodiamond with long spin-relaxation times. *Nat. communications* **6**, 8459 (2015).
21. M Cassidy, H Chan, B Ross, P Bhattacharya, CM Marcus, In vivo magnetic resonance imaging of hyperpolarized silicon particles. *Nat. nanotechnology* **8**, 363 (2013).
22. K Turcheniuk, VN Mochalin, Biomedical applications of nanodiamond. *Nanotechnology* **28**, 252001 (2017).
23. KK Liu, CL Cheng, CC Chang, JI Chao, Biocompatible and detectable carboxylated nanodiamond on human cell. *Nanotechnology* **18**, 325102 (2007).
24. Y Yuan, et al., Pulmonary toxicity and translocation of nanodiamonds in mice. *Diam. Relat. Mater.* **19**, 291–299 (2010).
25. CW Lam, JT James, R McCluskey, RL Hunter, Pulmonary toxicity of single-wall carbon nanotubes in mice 7 and 90 days after intratracheal instillation. *Toxicol. sciences* **77**, 126–134 (2004).
26. J Muller, et al., Respiratory toxicity of multi-wall carbon nanotubes. *Toxicol. applied pharmacology* **207**, 221–231 (2005).
27. AM Schrand, SAC Hens, OA Shenderova, Nanodiamond particles: properties and perspectives for bioapplications. *Critical reviews solid state materials sciences* **34**, 18–74 (2009).
28. A Puzyr, et al., Nanodiamonds with novel properties: a biological study. *Diam. Relat. materials* **16**, 2124–2128 (2007).
29. K Bakowicz, S Mitura, (wide bandgap materials in) medical and bio-physical applications-biocompatibility of ncd. *J. Wide Bandgap Mater.* **9**, 261–272 (2002).
30. S Rojas, JD Gispert, M M, H Alvaro, Mercedes anííííía, JR Herance, Biodistribution of amino-functionalized diamond nanoparticles. in vivo studies based on 18f radionuclide emission. *ACS nano* **5**, 5552–5559 (2011).

Xiaojun Lv, Jeffrey H. Walton, Emanuel Druga, Fei Wang, Alessandra Aguilar, Tommy McKnelly, Raffi Nazaryan, Fanglin Linda Liu, Lan Wu, Olga Shenderova, Daniel B. Vigneron, Carlos A. Meriles, Jeffrey A. Reimer, Alexander Pines

31. V Vaijayanthimala, et al., The long-term stability and biocompatibility of fluorescent nanodiamond as an in vivo contrast agent. *Biomaterials* **33**, 7794–7802 (2012).
32. XQ Zhang, et al., Multimodal nanodiamond drug delivery carriers for selective targeting, imaging, and enhanced chemotherapeutic efficacy. *Adv. materials* **23**, 4770–4775 (2011).
33. G Xi, et al., Convection-enhanced delivery of nanodiamond drug delivery platforms for intracranial tumor treatment. *Nanomedicine: Nanotechnology, Biol. Medicine* **10**, 381–391 (2014).
34. EK Chow, et al., Nanodiamond therapeutic delivery agents mediate enhanced chemoresistant tumor treatment. *Sci. translational medicine* **3**, 73ra21–73ra21 (2011).
35. D Ho, Nanodiamond modified gutta percha (ndgp) composite for non-surgical root canal therapy (rct) filler material. *Clin. Trials* (2020).
36. PW Goodwill, SM Conolly, The x-space formulation of the magnetic particle imaging process: 1-d signal, resolution, bandwidth, snr, sar, and magnetostimulation. *IEEE transactions on medical imaging* **29**, 1851–1859 (2010).
37. U Zurbuchen, et al., Determination of the electrical conductivity of human liver metastases: impact on therapy planning in the radiofrequency ablation of liver tumors. *Acta Radiol.* **58**, 164–169 (2017).
38. PR Zangara, et al., Dynamics of frequency-swept nuclear spin optical pumping in powdered diamond at low magnetic fields. *Proc. Natl. Acad. Sci.* **116**, 2512–2520 (2019).
39. A Ajoy, et al., Orientation-independent room temperature optical 13c hyperpolarization in powdered diamond. *Sci. Adv.* **4**, eaar5492 (2018).
40. ML Denton, et al., Damage thresholds for exposure to nir and blue lasers in an in vitro rpe cell system. *Investig. ophthalmology & visual science* **47**, 3065–3073 (2006).
41. MA Frey, et al., Phosphorus-31 mri of hard and soft solids using quadratic echo line-narrowing. *Proc. Natl. Acad. Sci.* **109**, 5190–5195 (2012).
42. K Takegoshi, C McDowell, A "magic echo" pulse sequence for the high-resolution nmr spectra of abundant spins in solids. *Chem. physics letters* **116**, 100–104 (1985).
43. MA Frey, et al., Phosphorus-31 mri of hard and soft solids using quadratic echo line-narrowing. *Proc. Natl. Acad. Sci.* **109**, 5190–5195 (2012).
44. EY Chang, J Du, CB Chung, Ute imaging in the musculoskeletal system. *J. magnetic resonance imaging* **41**, 870–883 (2015).
45. Thorlabs, apd410x operation manual, Technical report (2018).
46. J Tetienne, et al., Magnetic-field-dependent photodynamics of single nv defects in diamond: an application to qualitative all-optical magnetic imaging. *New J. Phys.* **14**, 103033 (2012).
47. Lightning-link rapid alexa fluor 647 conjugate data sheet, Technical report (2018).
48. A Bumb, et al., Wide-field background free imaging by magnetic modulation of nanodiamond fluorescence. *Biophys. J.* **106**, 796a (2014).
49. AS Merbach, L Helm, E Toth, *The chemistry of contrast agents in medical magnetic resonance imaging*. (John Wiley & Sons), (2013).

Xudong Lv, Jeffrey H. Walton, Emanuel Druga, Fei Wang, Alessandra Aguilar, Tommy McKnelly, Raffi Nazaryan, Fanglin Liu, Lan Wu, Olga Shenderova, Daniel B. Vigneron, Carlos A. Meriles, Jeffrey A. Reimer, Alexander Pines